ELSEVIER

J. Non-Newtonian Fluid Mech. 88 (1999) 63–88

Journal of Non-Newtonian Fluid Mechanics

www.elsevier.com/locate/jnnfm

Plane contraction flows of upper convected Maxwell and Phan-Thien–Tanner fluids as predicted by a finite-volume method

P.J. Oliveira[a,*], F.T. Pinho[b]

[a]*Departamento de Engenharia Electromecânica, Universidade da Beira Interior, 6200 Covilhã, Portugal*
[b]*Centro de Estudos de Fenómenos de Transporte, Faculdade de Engenharia Universidade do Porto, Rua dos Bragas, 4099 Porto Codex, Portugal*

Received 4 August 1988; received in revised form 4 February 1999

Abstract

A finite-volume (FV) procedure is applied to the prediction of two-dimensional (2-D) laminar flow through a 4 : 1 planar contraction of upper convected Maxwell (UCM) and simplified Phan-Thien–Tanner (SPTT) fluids. The method incorporates general coordinates, indirect addressing for easy mapping of complex domains, and is based on the collocated mesh arrangement. Calculations with the UCM model at a Reynolds number of 0.01 were carried out with three consecutively refined meshes which enabled the estimation of the accuracy of the predictions of the main vortex characteristics through Richardson's extrapolation. Converged solutions with the first-order upwind differencing scheme for the convective terms were obtained up to at least $De = 8$ in the finest mesh, but were limited to $De \leq 1$, $De \leq 3$ and $De \leq 5$ for the fine, medium and coarse meshes, respectively, when using the second-order linear upwind scheme. The predicted flow patterns for increasing Deborah numbers with the UCM model resemble the well known lip vortex enhancement mechanism reported in the literature for constant-viscosity fluids in axisymmetric contractions and shear-thinning fluids in planar contraction, but very fine meshes were required in order to capture the described vortex activity. Predictions with the SPTT model also compared well with the behaviour reported in the literature.

Keywords: Sudden contraction; Viscoelastic; Collocated mesh; Finite-volume; Lip vortex

1. Introduction

The sudden contraction flow of viscoelastic fluids has been one of the most extensively investigated viscoelastic flows, with particular attention paid to the different flow patterns which may arise near the re-entrant and salient corners. In this respect, the size and the shape of the large vortex found upstream

* Corresponding author. Fax: +351-75-320820
E-mail addresses: pjpo@ubi.pt (P.J. Oliveira); fpinho@fe.up.pt (F.T. Pinho)

0377-0257/99/$ – see front matter
PII: S0377-0257(99)00017-8

of the plane of the contraction depend strongly on (i) the elasticity of the fluid, as quantified by the Weissenberg or Deborah numbers, (ii) the type of contraction (round or plane), (iii) the contraction ratio and (iv) the Reynolds number.

The investigation of sudden contraction flows has been initiated in the last century, and by now, their characteristics are well known for Newtonian and purely viscous shear-thinning fluids, as shown in the review of Boger [1]. Most of the research has considered the circular geometry, but planar contractions have also been under scrutiny.

The picture is rather less clear and more complicated when viscoelastic fluids are concerned. From an experimental point of view, it is difficult to isolate the rheological characteristics of the fluids, and elasticity is frequently associated with shear-thinning and manifests itself in various ways, such as normal stress effects in steady shear, high storage modulus effects in transient flows as well as high elongational viscosity effects, all these properties occurring in various degrees and combinations. On the other hand, it is easier to isolate these effects in numerical investigations by a proper selection of constitutive models, but here too, progress has been slow due to convergence difficulties associated with high elastic stresses in sharp corners.

The relevance of flows in contractions stems not only from its application to rheology, where it can provide valuable information on the extensional characteristics of fluids [2], but also from its application in industrial processes like extrusion. In addition, the combination of geometric simplicity with flow complexity provides a convenient problem for the development and the assessment of numerical methods in non-Newtonian fluid mechanics.

Contraction flows are very sensitive to fluid elasticity and viscosity as well as to the contraction ratio. Under certain circumstances, various flow patterns are observed, the typical example being the corner vortex behaviour of Boger fluids in circular and planar contraction. In the former, a strong corner vortex enhancement is observed with the Deborah number [3], usually preceded by the formation of a lip vortex. In the latter geometry, the corner vortex enhancement and the lip vortex mechanism have been more difficult to discern [4], and when observed, they have been less intense. However, for high contraction ratios (16 : 1 and 80 : 1), the lip-vortex mechanism for vortex enhancement has been found to take place, where fingering of the salient corner vortex towards the re-entrant corner has sometimes been observed, followed by the appearance of a small but strong lip vortex. This vortex grows with fluid elasticity, and may merge and overcome the initial salient corner vortex. Then, the merged vortices would be enhanced by fluid elasticity.

The latter experiments of Evans and Walters [5] in the 4 : 1 (almost) planar contraction have confirmed that the lip-vortex mechanism of vortex enhancement also does occur at the lower contraction ratios for shear-thinning fluids, provided an adequate choice of fluid rheology and flow rate is made. In both round and planar cases, the centre of the enhanced corner vortex approached the re-entrant corner, and similar complex effects, strongly dependent on boundary conditions, were also reported. The fact that lip vortices could not be observed in the planar geometry with constant-viscosity elastic fluids, but were clearly present in the circular case, remains unexplained in spite of some theoretical work [6]. It is in contrast to the present predictions and also to some recent predictions reported in the literature, which are discussed below.

Two possible causes for this discrepancy could be

1. the geometry used by Evans and Walters [5] is not representative of two-dimensional (2-D) planar flow, and presumably, secondary motions would destroy the lip vortex formation, and

2. the visualizations in the square cross-sectional upstream channel were not taken at the appropriate Deborah/Reynolds number range (the simulations show that the lip vortex exists only in a restricted, rather low range of Deborah numbers, depending on the Reynolds number).

Other relevant experimental work in planar 4 : 1 contractions were conducted by White and Baird [7] and Quinzani et al. [8]. The former authors observed a lip vortex and reported corner vortex enhancement for low density polyethylene (LDPE) melts, whereas polystyrene (PS) melts gave negligible vortex enhancement for the flow rates utilised. In a later work, the same authors [9] simulated the experiments with the exponential PTT model using $\xi = 0.25$ and $\varepsilon = 0.01$ for the LDPE, and $\varepsilon = 0.1$ for the PS. Since low ε brings the PTT model closer to the upper convected Maxwell (UCM) or to the Oldroyd-B model, it may be presumed from [7,9] that corner vortex enhancement and lip vortex formation should be expected for the UCM fluid.

The first numerical simulations of the contraction flow were far from predicting the observed flow patterns for a number of reasons. The constitutive models used by Crochet and Pilate [10], and Perera and Walters [11] were too simple and thus unable to predict the elongational viscosity effects which had been observed and known to be important. Adoption of simple differential constitutive equations, such as the UCM and the Oldroyd-B models led to the first numerical difficulties: the iterative calculations failed to converge at low Weissenberg or Deborah numbers. Various attempts at solving this problem have been reported in connection with the finite-element method [12–14]. Great improvements were achieved through the introduction of elements with higher and mixed degrees of freedom and the use of Petrov–Galerkin or some other form of streamline upwind (SUPG or SU) weighting [12]. Additional improvements arose from a better decoupling of elastic and viscous effects, and from a tighter control of these two characteristics, as is the case with the elastic-viscous stress-splitting (EVSS) method of Rajagopalan et al. [13]. Pressure correction techniques borrowed from finite-volume (FV) methods have been incorporated into SUPG finite-element methods by Carew et al. [14], and this has, very recently, gained improved stability with the recovery scheme of Matallah et al. [15] (here, velocity gradients in the constitutive equations are 'smoothed' in some manner).

The next step was the utilisation of more realistic constitutive equations, and fortunately, it has been found that, in spite of their higher complexity, these models are less stringent from a numerical point of view [16]. Hence UCM and Oldroyd-B models are deemed adequate for the development and the improvement of methods that may evolve at a later stage to more realistic and numerically less demanding constitutive equations. Examples of the application of complex rheological equations are the works of Purnode and Crochet [17], who used the FENE-P model to simulate many of the features observed by Evans and Walters [4,5], such as the appearance and the growth of the lip vortex, and those of White and Baird [9], Carew et al. [14], and very recently, Xue et al. [18,19], who used various forms of the Phan-Thien–Tanner (PTT) model.

The 'leitmotiv' which prompted the present paper was the fact that on early simulations of the contraction flow of an UCM fluid [20], the results did not quite agree with some (not to say most) of the previously published numerical work on planar contraction flows in which the flow of UCM fluids appears to be very similar to that of Newtonian fluids and does not exhibit the lip vortex as well as vortex growth with fluid elasticity [12,21–23]. In particular, in their important paper, Marchal and Crochet [12] argued that the main features of the flow of an UCM fluid are little affected by the amount of elasticity and that the small lip vortex that they found in some of their calculations is, most probably, a numerical artifact. It is interesting to remark that predictions by the same authors in a previous paper

[24] showed lip vortices for the planar contraction flow, but the absence of lip vortices on the axisymmetric case for an Oldroyd-B fluid. Thus, there appears to exist an inconsistency in the results of these two papers, a common feature in both works [12,24] being the coarseness of the mesh. In [20], we did predict the existence of lip vortex in the planar contraction, and that has been corroborated by the very recent Boger fluid predictions of Matallah et al. [15] and Xue et al. [18,19], who used finite-element and finite-volume methods, and who have also shown that the Oldroyd-B constitutive equation can lead to the appearance of a lip vortex in the 2-D contraction flow, provided the computational mesh is sufficiently fine. We have thus an independent and a parallel validation of our results. These seem to show that a lip vortex will always exist for the UCM fluid before the corner vortex starts its enhancement behaviour when the Deborah number is increased at fixed Reynolds number.

The objective of this work is to address this question in more detail with the general FV method developed by Oliveira et al. [25] and to assess the effects that mesh refinement and different discretisation schemes may have on the predicted flow patterns. The present FV method is able to provide converged solutions for higher Deborah number flows than in previous studies. Here, we go up to $De = 8$ with $Re = 0.01$ in a very fine mesh of more than 14 000 cells (elements) with a minimum non-dimensional spacing of 0.01, and where mesh spacing varies less than 5% between adjacent cells in the vicinity of the contraction plane. The method solves the flow and constitutive equations sequentially in a collocated mesh arrangement where all dependent variables are evaluated at the centre of the control volumes, and where both first- and second-order accurate differencing schemes are used to represent the convective terms. Here, this FV method is extended to cater to more complex constitutive equations, and predictions pertaining to the same flow geometry are also included for the case of a fluid obeying the simplified PTT constitutive equation in which the function of the trace of the stress tensor is linear.

In the following sections, the governing equations are given, the calculation method is outlined, and the results are presented and discussed. The paper ends with a summary of the main findings.

2. Governing differential equations

The basic equations are those for three-dimensional (3-D), incompressible and isothermal, laminar flow of the viscoelastic simplified PTT (SPTT) fluid, namely the continuity equation, the momentum equation and the SPTT constitutive equation. In general, these equations are written in curvilinear, non-orthogonal coordinates (ξ_l), but components of vectors and tensors are still referred to the original Cartesian (x_i) frame. To distinguish between these directions, we use the indices i, j and k for the Cartesian components, and l, m and n for the curvilinear directions, and summation is implied for repeated indices.

The continuity equation is

$$\frac{\partial u_i}{\partial x_i} = 0 \tag{1}$$

and the momentum conservation equation is

$$\frac{\partial \rho u_i}{\partial t} + \frac{\partial \rho u_j u_i}{\partial x_j} - \frac{\partial}{\partial x_j}\left(\eta \frac{\partial u_i}{\partial x_j}\right) = -\frac{\partial p}{\partial x_i} + \frac{\partial \tau_{ij}}{\partial x_j} + \rho g_i - \frac{\partial}{\partial x_j}\left(\eta \frac{\partial u_i}{\partial x_j}\right) \tag{2}$$

where a diffusion term is added and subtracted so that the FV method can be applied to equations retaining standard convection/diffusion form. The procedure does not affect the final steady state solution because both terms are dealt with consistently in space (see Section 3), and departs (apparently) from the usual practice in non-Newtonian calculations (the EVSS formulation) [13], where the stress tensor is splitted into Newtonian/solvent and elastic/polymer contributions, and the viscous contribution is made to appear explicitly in the momentum equation. A possible advantage is that, in this way, the calculation method remains completely general, regardless of the specific features of the adopted constitutive equation. On the other hand, a close inspection shows that this approach is indeed very similar to the EVSS, if not totally equivalent.

The extra stress tensor τ_{ij} is given by the constitutive equation for the simplified PTT model fluid:

$$\left(1+\frac{\varepsilon\lambda}{\eta}\tau_{kk}\right)\tau_{ij}+\lambda\left(\frac{\partial\tau_{ij}}{\partial t}+u_k\frac{\partial\tau_{ij}}{\partial x_k}\right)=\eta\left(\frac{\partial u_i}{\partial x_j}+\frac{\partial u_j}{\partial x_i}-\frac{2}{3}\frac{\partial u_k}{\partial x_k}\delta_{ij}\right)+\lambda\left(\tau_{jk}\frac{\partial u_i}{\partial x_k}+\tau_{ik}\frac{\partial u_j}{\partial x_k}\right) \tag{3}$$

which reduces to the UCM fluid model when the material parameter ε is set to zero. The full PTT model is based on the Gordon–Schowalter (GS) convected derivative [26], which reduces to the upper convective derivative when the ξ parameter of the GS derivative is set to zero. In this work, the linear form of the stress coefficient is used in the SPTT model. Here, λ is the relaxation time, η the viscosity coefficient and the two-thirds term on the right-hand side of Eq. (3) is zero for the incompressible liquids analysed here, but it is kept because it is not exactly zero in the numerical approximation and because it has been found to improve the accuracy and the convergence rate in the Newtonian calculation. This term is a part of a complete formulation of the constitutive equations [27] and originates in the viscous contribution of the constitutive model. It should not be seen as a compressibility factor, but rather as a correction which assures that the trace of the stress tensor in the FV equations does vanish. The parameter ε controls the magnitude of the extensional viscosity which increases as this parameter is reduced.

In Eqs. (2) and (3), we adopt the notation of writing on the left-hand side the terms which are treated implicitly in the numerical procedure, whereas those on the right-hand side are dealt with explicitly, i.e. they are included in the so-called source term.

3. Finite-volume numerical method

The transport equations for mass and momentum conservation, and for the rheological model are transformed into a general non-orthogonal coordinate system before being discretised. The simplified PTT constitutive Eq. (3), for example, can be written in a compact form in such a coordinate system as

$$\begin{aligned}\left(1+\frac{\varepsilon\lambda}{\eta}\tau_{kk}\right)J\tau_{ij}+\lambda\frac{\partial}{\partial t}(J\tau_{ij})+\lambda\frac{\partial}{\partial\xi_l}(\beta_{lk}u_k\tau_{ij})=\eta\left(\beta_{lj}\frac{\partial u_i}{\partial\xi_l}+\beta_{li}\frac{\partial u_j}{\partial\xi_l}\right)\\ +\lambda\left[(\beta_{lk}\tau_{kj})\frac{\partial u_i}{\partial\xi_l}+(\beta_{lk}\tau_{ki})\frac{\partial u_j}{\partial\xi_l}\right]-\frac{2}{3}\eta\beta_{lk}\frac{\partial u_k}{\partial\xi_l}\delta_{ij}\end{aligned} \tag{4}$$

These transformations are a necessary step towards using a general FV method based on the collocated mesh arrangement, as described in [25], even if the problem in question does not require non-orthogonal coordinates as in the case here. The reader is referred to [25] for the

other equations and a more detailed description of the numerical method. Here, only a brief outline of the method is given.

In the FV method, the computational domain is divided into contiguous six-faced cells for the general 3-D case, and the differential equations are integrated over each cell [28]. A collocated mesh arrangement is used in which all variables are stored at the centre-of-cell location, thus avoiding the need to calculate stresses at geometrical singular points, such as the re-entrant corner. In general, all terms in the equations are discretised by means of central differences except the convection terms which are approximated by either the linear-upwind differencing scheme (LUDS) or the upwind differencing scheme (UDS). In the UDS scheme, the value of a convected variable at the face of a control volume is given by its value at the first upstream cell centre, whereas in the LUDS scheme, the value of that convected variable at the same cell face is given by linear extrapolation based on the values of the variable at the two upstream cells. The end result of discretisation is a set of linearised algebraic equations relating centre-of-cell values of the unknown variables (u_i, p, τ_{ij}) to their values at nearby cells. These sets are solved by standard conjugate-gradient methods for linear sets of equations.

The notation is kept as general as possible, following Oliveira et al. [25]. In discretization, the β_i coefficients are replaced by area components of the surface whose normal vector points towards direction l denote B_{li}, the Jacobian J is replaced by the cell volume V, and the derivatives $\partial/\partial\xi_l$ become differences between values along direction l. A stencil of the control volume and neighbouring cells is shown in Fig. 1.

The discretised continuity equation reflects mass conservation for each cell P:

$$\sum_{\mathrm{f}=1}^{6} F_{\mathrm{f}} = 0 \quad \text{with} \quad F_{\mathrm{f}} = \sum_{j} \rho B_{\mathrm{f}j}^{\mathrm{f}}\, \tilde{u}_{j,\mathrm{f}} \tag{5}$$

where F_{f} stands for outgoing mass flow rates at cell face f and $\tilde{u}_{j,\mathrm{f}}$ refers to the cell face velocity component u_j, with the tilde stressing that this velocity cannot be computed from simple linear interpolation, but needs to be evaluated via a Rhie and Chow's [29] interpolation to ensure coupling between velocity and pressure.

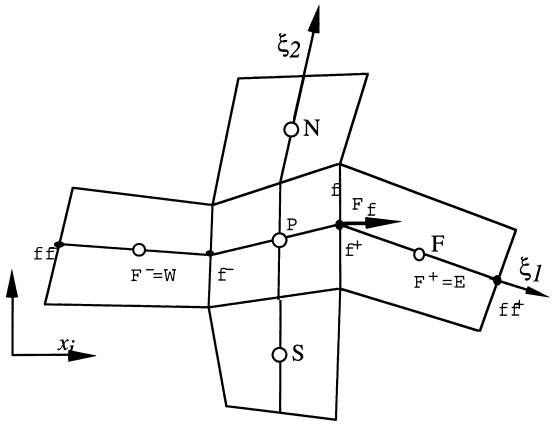

Fig. 1. Representation of the computational molecule in 2-D and some nomenclature. For 3-D, add corresponding bottom B and top T cells.

The discretised i-momentum equation results from the integration of Eq. (2) and has the form

$$a_{\mathrm{P}} u_{i,\mathrm{P}} - \sum_F a_F u_{i,F} = S_{u_i} + \frac{\rho V_{\mathrm{P}}}{\delta t} u^0_{i,\mathrm{P}} \tag{6}$$

where u^0_i refers to the velocity of the previous time level and the coefficients of the neighbouring cells (a_F, with F spanning the near-neighbouring cells of cell P) have convective (a^{C}_F) and diffusive (a^{D}_F) contributions:

$$a_F = a^{\mathrm{D}}_F + a^{\mathrm{C}}_F, \quad \text{with} \quad a^{\mathrm{D}}_F = \frac{\eta_{\mathrm{f}} B^2_{\mathrm{f}}}{V_{\mathrm{f}}} \quad \text{and} \quad a^{\mathrm{C}}_F = \max(F_{\mathrm{f}}, 0) \tag{7}$$

The convective contributions in Eq. (7) are valid when the upwind scheme is adopted, and the reader is referred to Oliveira et al. [25] for expressions pertaining to the linear-upwind scheme. The central coefficient in Eq. (6) is

$$a_{\mathrm{P}} = \frac{\rho V_{\mathrm{P}}}{\delta t} + \sum_F a_F \tag{8}$$

and the total source term S_{u_i} has contributions from all the terms on the right-hand side of Eq. (2), namely from the pressure gradient, the stress-divergence, gravity and the added diffusion flux:

$$S_{u_i} = S_{u_i,\mathrm{pressure}} + S_{u_i,\mathrm{gravity}} + S_{u_i,\mathrm{stress}} + S_{u_i,\mathrm{diffusion}} \tag{9}$$

In Section 2, we stressed that the two added diffusive fluxes are dealt with in a consistent manner: they are discretised in the same way using central differences, and then, the term on the left-hand side of Eq. (2) is treated implicitly giving rise to the a^D_F coefficients in Eq. (7), whereas the term on the right-hand side is incorporated into the source term and treated explicitly. As a steady state solution is approached, these two terms cancel out exactly.

The discretised constitutive equation is also casted into a similar algebraic form as

$$a^{\tau}_{\mathrm{P}} \tau_{ij,\mathrm{P}} - \sum_F a^{\tau}_F \tau_{ij,F} = S_{\tau ij} + \frac{\lambda_{\mathrm{P}} V_{\mathrm{P}}}{\delta t} \tau^0_{ij,\mathrm{P}} \tag{10}$$

with the stress related coefficients a^{τ}_F given only by convective contributions

$$a^{\tau}_F = \max\left(\frac{\lambda}{\rho} F_{\mathrm{f}}, 0\right) \tag{11}$$

when the upwind scheme is adopted, and the central coefficient now being defined by

$$a^{\tau}_{\mathrm{P}} = V_{\mathrm{P}}\left(1 + \frac{\varepsilon \lambda_{\mathrm{P}}}{\eta_{\mathrm{P}}} \tau_{kk,\mathrm{P}}\right) + \sum_F a^{\tau}_F + \frac{\lambda_{\mathrm{P}} V_{\mathrm{P}}}{\delta t} \tag{12}$$

In Eq. (12), $\tau_{kk,\mathrm{P}}$ represents the trace of the stress tensor for cell P, an invariant quantity evaluated from stress field values at the previous time level. Since this quantity is large and positive, especially near geometrical singular points, its incorporation into the a^{τ}_{P} coefficients greatly enhances the numerical stability of the iteration procedure for the τ_{ij} equations.

The two-thirds term in the Newtonian part of the stress tensor is also dealt with consistently in space, meaning that it is discretised in the same way as the other viscous terms of the constitutive equation. Hence, for a purely Newtonian fluid, the trace of the stress tensor will be exactly zero when a converged solution is attained. We emphasize that in the constitutive equation, no additional stress diffusion terms have been added to improve stability, as is often the case in other FV methods [30,18,31].

The convective coefficients in the momentum and constitutive equations involve the six neighbouring cell values surrounding the central cell P when the UDS scheme is used, and additional neighbours to these neighbour cells (denoted as far-neighbours) when the LUDS scheme is used instead (c.f. Fig. 1 and [25]; in this case, the stencil has six near-neighbour and six far-neighbour cells).

To ensure coupling between pressure and velocity, a form of the Rhie and Chow [29] scheme is used to evaluate the mass flow rates, as given by Issa and Oliveira [32]. Furthermore, for coupling the stress and the velocity fields, the special interpolation technique developed by Oliveira et al. [25] is applied to evaluate all the face stresses required in the divergence of the stress tensor terms in the momentum equation, i.e.

$$S_{u_i,\text{stress}} = \sum_{\text{f}} \sum_{j} B_{\text{f}i}\, \tilde{\tau}_{ij,\text{f}} \tag{13}$$

in Eq. (9).

The solution procedure follows a modified version of the SIMPLEC algorithm of Van Doormal and Raithby [33]. The procedure has been extended to include the solution of the non-Newtonian constitutive equation and has three major steps:

1. initially, the six constitutive equations are solved implicitly for the stress components τ_{ij}. This is done just prior to the first time the three momentum equations are handled since these require knowledge of the stress field;
2. then, the three momentum equations are solved implicitly for each velocity component, u_i^*; and
3. as the calculated velocity components u_i^* do not generally satisfy the continuity equation, the third step of the algorithm involves a correction to u_i^* and to the pressure field p^*, so that an updated velocity field u_i^{**} and the corrected pressure field p^{**} will satisfy simultaneously the continuity and the momentum equations.

Boundary conditions are required for the dependent variables at the boundary faces of the computational domain. At the inlet boundary face located far upstream of the contraction region, the streamwise velocity component and the shear and the normal stress components were set equal to fully developed values and all other quantities were set to zero. For the shear-thinning PTT fluid, the stress field used at the inlet was also that given by the corresponding UCM ($\varepsilon = 0$), but in all cases, the inlet was sufficiently far upstream for this localised inconsistency to have any effect farther downstream. This was confirmed in the numerical experiments and is also apparent from the streamline patterns. The outlet boundary face was located far from the contraction plane, where the flow is locally parabolic, and thus the streamwise gradients for velocity, stress and pressure gradients could be safely set to zero without perturbing the upstream flow conditions.

Due to symmetry, only half of the physical domain was selected for the calculations. Across the symmetry plane thus created, the convective and tangential diffusive fluxes must vanish and this was imposed by means of reflection laws as explained in [25].

At the solid walls, the no-slip condition applies to all the velocity components and pressure is linearly extrapolated from the two nearest neighbour cells, a practice used in classical Newtonian CFD (see [34]). The stress components, on the other hand, are given implicitly by a relation derived from the constitutive equation after equating the convective terms to zero and considering that velocity differences evaluated in the plane coincident with the wall must vanish (i.e. $\partial u_i/\partial \xi_l = 0$ for $l \neq$ f, where f is the direction normal to the wall).

We finally remark that the use of a general semi-structured method based on non-orthogonal collocated grids, together with indirect addressing of the cells, removes the inherent complications of orthogonal structured meshes when simulating complex geometries, namely the need for larger amounts of computer memory and special procedures to render inactive the cells falling outside the flow domain. The quantify this point, if the present problem was solved without indirect addressing, an overhead of 49.3% in wasted computer memory would be required, not to mention the inherent increase in computer time. In this respect, this formulation represents a major improvement on current FV methods for viscoelastic flow predictions, even when considering the most recent FV methods reported in the literature (e.g. [18,30]).

The accuracy of the overall method is controlled by the lower-order scheme utilised, and thus is nominally first-order when the UDS is used to represent the convective terms, and second-order when the LUDS is used instead (this is often mentioned in the literature as the second-order upwind SOU scheme). Note also that the remaining terms of the Oldroyd upper convected derivative are always evaluated by means of the second-order central differencing scheme (CDS). Finally, when simulating $De = 0$ flows, CDS can be (and was) used for the convective terms of the momentum equations. For $De > 0$, however, CDS is unable to represent the convective terms in the stress equation since it is devoid of a diffusion term, and CDS alone would, inevitably, lead to an oscillatory solution.

4. Flow geometry and computational mesh

The problem under consideration is the flow in a 4 : 1 planar contraction as sketched in Fig. 2. Fig. 2 defines the coordinate system and nomenclature, and indicates the structured blocks used to generate the computational meshes.

The calculation domain for the base case spans from -20 to $+50$ downstream channel half-heights H_2 in the longitudinal direction. The upstream length ($L_1 = 20H_2$) was found to be sufficient for the inlet fully developed profiles to be maintained for some distance before the contraction and for fully developed stress conditions to be established for the SPTT fluid, whereas the downstream length

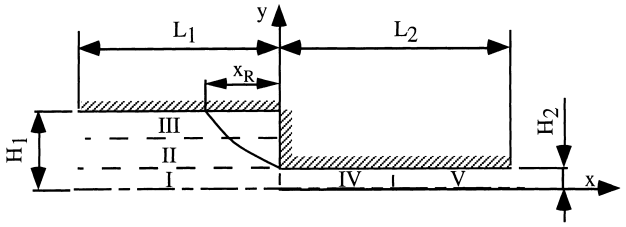

Fig. 2. Schematic representation of the 4 : 1 planar contraction.

($L_2 = 50H_2$) is sufficient for the flow at the contraction plane to remain unaffected by outlet conditions and for the flow to become locally parabolic near the exit for the present Reynolds numbers. Computational domains with $L_1 = 10H_2$ and $L_2 = 10H_2$ were also used in initial calculations and the vortex features were found to remain almost unaffected. The Reynolds and Deborah numbers are defined on the basis of downstream channel quantities

$$\mathrm{Re} = \frac{\rho U_2 H_2}{\eta} \tag{14}$$

$$\mathrm{De} = \frac{\lambda U_2}{H_2} \tag{15}$$

and they were varied independently by changing the parameters η and λ, respectively.

These definitions are in agreement with those in the experimental and numerical works listed in Table 1, which summarises the corresponding flow conditions, although the fluids utilised may differ. With the above definitions for the non-dimensional numbers, our simulations can be compared to the results obtained by the authors listed in Table 1 for the same values of the Reynolds and Deborah numbers.

The present simulations with the UCM fluid were mainly obtained for a Reynolds number of 0.01 (closely representative of creeping flow), but a few cases were run for Re = 0, 0.36 and 1.0,

Table 1
Some results in the literature for the planar 4 : 1 contraction flow

Reference	Work	Fluid	De $= \lambda U_2/H_2$	Re $= \rho H_2 U_2/\eta$	$\delta x/H_2$
[4]	Exp.[a]	polyacrylamide in maltose syrup + water	$\leq$64	0.00003–6.37	–
[5]	Exp.	0.2–1% polyacrylamide in water	not quoted	not quoted	–
[8]	Exp.	polyisobutylene in tetradecane	0.4–4.15	0.04–0.4	–
[21]	Num.[b]	UCM	$\leq$2	$\leq$2.1	1/8
[12]	Num.	Oldroyd-B: $\lambda_2/\lambda_1 = 1/9$	4.7	creeping flow	0.092
			$\leq$6.7	–	–
[22]	Num.	Oldroyd-B: $\lambda_2/\lambda_1 = 1/9$, 1/5, and 1/8	$\leq$1.04 ($\lambda_2/\lambda_1 = 1/9$)	creeping flow	1/16
			$\leq$1.10 ($\lambda_2/\lambda_1 = 1/8$)	–	–
[14]	Num.	Oldroyd-B: $\lambda_2/\lambda_1 = 1/9$;	$\leq$2	1	$\approx$1/7
		PTT $\varepsilon = 0.02$, and 0.25; $0 < \xi < 0.2$	$\leq$15	1	–
[23]	Num.	Oldroyd-B: $\lambda_2/\lambda_1 = 1/9$	$\leq$2	0.01, 0.1 and 1	0.025
[16]	Num.	PTT; $\varepsilon = 0.02$, 0.15, 0.2, and 0.25	$\leq$25	1	$\approx$1/7
			($\leq$2 for Oldroyd-B)	–	–
[17]	Num.	FENE-P	as in [4]	as in [4]	–
[18]	Num.	UCM;	$\leq$2.75	–	0.014
		Oldroyd-B: $\lambda_2/\lambda_1 = 1/8$;	$\leq$4.4	0.6	–
		PTT	<4.15	2.1	–
[19]	Num.	UCM; PTT; $\varepsilon = 0.25$; $0 < \xi < 0.15$	$\leq$7.2	0.01–0.1	0.014
[15]	Num.	Oldroyd-B: $\lambda_2/\lambda_1 = 1/9$	$\leq$4	creeping flow	$\approx$1/7
				and Re = 1	
This work	Num.	UCM; PTT; $\varepsilon = 1$, and 0.25	$\leq$8 (10 in coarse mesh)	0.01 and 1	0.01

[a] Exp.: Experimental investigation.
[b] Num.: Numerical investigation.

while the Deborah number varied from 0 to 8, clearly in excess of the maximum values obtained by Yoo and Na [22], Marchal and Crochet [12], and more recently, by Matallah et al. [15] and Xue et al. [18,19], with the added consideration that the meshes here are much finer. For the base case ($Re = 0.01$), solutions were obtained with UDS up to $De = 8$, and with LUDS for $De \leq 1$ in all the three meshes. In the range $1 \leq De \leq 3$, numerical solutions with LUDS were restricted to the coarse and medium meshes, and for higher elasticity, namely $3 < De \leq 5$, solutions with LUDS could only be obtained in the coarse mesh. It may thus be concluded that the higher-order LUDS scheme suffers from numerical instability problems at high Deborah numbers. The cause for this behaviour may reside in the absence of delimiters in this scheme (compared to total-variation-diminishing TVD schemes). So, in order to improve the accuracy of the calculations at high De, and since convection had to rely on the first-order UDS scheme, it was decided that very fine meshes be used instead.

For the PTT model, calculations were performed at a Reynolds number of 0.01 and at a Deborah number of 2, with ε taking values of 0.1 and 0.25. A higher Reynolds number of 0.36 was also investigated with the PTT model to assess the effect of this number and to facilitate the comparison with the measurements of Quinzani et al. [8].

The 2-D geometry was divided into five blocks used to generate computational meshes (see Fig. 2), with blocks I to III in the inlet channel and blocks IV and V in the outlet channel. The cells were made smaller as the contraction plane, the upstream channel wall and the re-entrant corner were approached, using appropriate expansion or contraction geometrical factors. These are defined for each direction as the ratio of two consecutive cell lengths (e.g. for a Cartesian grid, $f_x = \delta_{x_{i+1}}/\delta_{x_i}$ with δ_{x_i} being the length of cell i in the x-direction). In this way, the minimum normalised cell size at the corner was $\delta_{x\min}/H_2 = \delta_{y\min}/H_2 = 0.01$ for the finest mesh, mesh 3, $\delta_{x\min}/H_2 = \delta_{y\min}/H_2 = 0.02$ and $\delta_{x\min}/H_2 = \delta_{y\min}/H_2 = 0.04$ for the two coarser meshes, meshes 2 and 1, respectively. Here, mesh refinement was carried out by halving the cell widths in each direction to facilitate the assessment of mesh convergence and accuracy via the application of Richardson's extrapolation to the limit. We emphasize that mesh 3 is one of the finest meshes used so far in this benchmark problem, and it must be measured not only by the smallest normalised mesh spacing (here, of 0.01), but also by the maximum expansion ratio for cell size variation between adjacent cells, which here is as low as 5% in the region of interest. This 2-D mesh has a total of 14 258 cells (or elements).

A summary of the main characteristics of the computational meshes is presented in Table 2 and an idea of the resolution of the finer mesh can be grasped from Fig. 3.

All the results to be given below were computed with the finest mesh (mesh 3) unless otherwise stated. A study of the effect of mesh refinement and differencing scheme is given in Section 5.

5. Results and discussion

Since the interest from the outset was to verify how the flow pattern of a UCM fluid in a 4 : 1 planar contraction changes with fluid elasticity, and specifically, to verify whether lip vortices and vortex enhancement do occur, we start by presenting in Fig. 4 the predicted streamlines for Deborah number flows from 0 to 8 at a Reynolds number of 0.01.

Simulations were actually performed up to the Deborah number of 10, but were not pursued further due to the long calculation times required. We are, therefore, unable to answer the question as to

Table 2
Main mesh characteristics (domain is $L_1 = 20H_2$ and $L_2 = 50H_2$)

	Block I			Block II			Block III			Block IV			Block V			NC[a]
	NX × NY	f_x	f_y	NX × NY	f_x	f_y	NX × NY	f_x	f_y	NX × NY	f_x	f_y	NX × NY	f_x	f_y	
Mesh 1	24 × 10	0.8210	0.8475	24 × 13	0.8210	1.2091	24 × 5	0.8210	0.7384	20 × 10	1.2179	0.8475	7 × 10	1.3782	0.8475	942
Mesh 2	47 × 20	0.9061	0.9206	47 × 25	0.9061	1.0996	47 × 9	0.9061	0.8593	40 × 20	1.1036	0.9206	13 × 20	1.1740	0.9206	3598
Mesh 3	94 × 40	0.9519	0.9595	94 × 50	0.9519	1.0486	94 × 17	0.9519	0.9270	80 × 40	1.0505	0.9595	25 × 40	1.0835	0.9595	14258

[a] NC: Total number of control-volumes or cells.

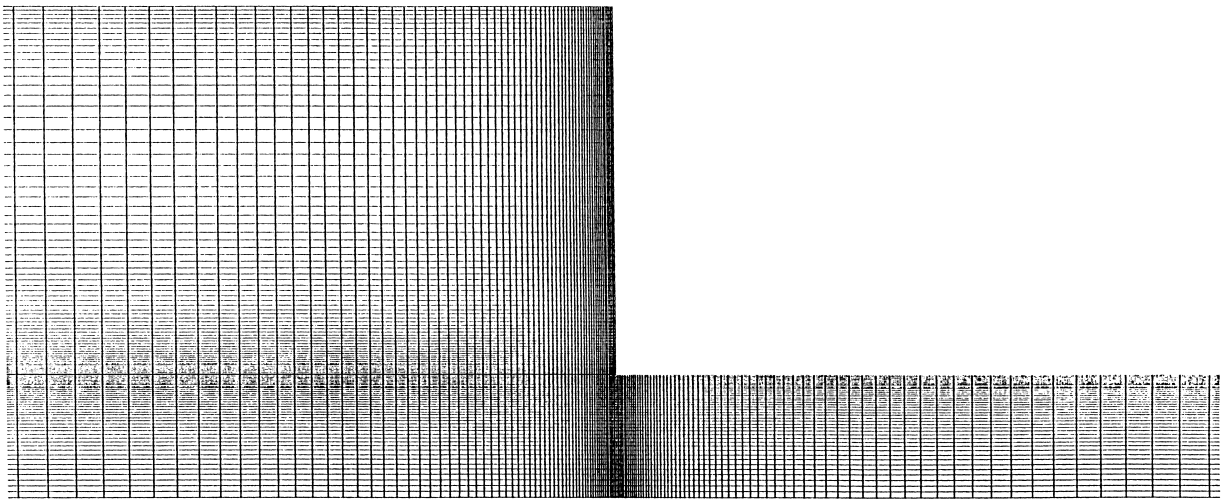

Fig. 3. The fine mesh (mesh 3) used in the calculations.

whether De = 10 is a limiting point, but the indication is that the calculations could be pursued for higher Deborah numbers.

The streamlines in Fig. 4 were based on calculations where the UDS discretization scheme was used for the convective terms after assessing its effects upon the predictions in terms of mesh refinement and discretization scheme (to be shown later). In the case of Newtonian flow, the recirculation length normalised as $x_R/2H_1$ was equal to 0.187, in agreement with the results reported by Sato and Richardson [23] and Xue et al. [18].

Fig. 4 shows that in the range De $\leq$ 2, there is a slight decrease in both the size and the intensity of the salient corner vortex as fluid elasticity is raised. Here, vortex size is measured by its non-dimensional length ($X_R = x_R/H_2$) and the intensity is measured by the maximum amount of recirculating flow relative to the inlet flow rate (thus the intensity $\Psi_R = \Psi_{max} - 1$, where Ψ_{max} is given by the code). In Fig. 4, the streamlines inside the vortices are spaced equally and so provide an indication of the vortex intensity and allow comparison between the various De flow cases. At De $\approx$ 1, a small lip vortex is already formed at the re-entrant corner. As the Deborah number is increased from 1 to 2, the lip vortex increases in size and strength, the salient corner vortex fingers towards the re-entrant corner, and eventually a separating streamline envelops the two vortices. In this range of Deborah numbers, the boundary of the recirculation region has a typical straight or concave shape, which becomes more concave when the two vortices are present. These findings are in agreement with the recent numerical results of Matallah et al. [15] and Xue et al. [18,19], but are not supported by the earlier visualisations of Evans and Walters [4].

Now, further increase in the Deborah number reverses the vortex behaviour with an increase in the size and the intensity of both the salient corner and the lip vortices until, eventually, a single vortex remains. In fact, at De = 2 and De = 3, the two vortices are clearly outlined in the streamline plots, whereas at De = 4, the merging process is complete, the plots suggesting that the lip vortex may have dominated the final stages of the merging process. For De > 4, there is a single strong recirculating region which grows with the Deborah number, the so-called vortex enhancement mechanism mentioned in Section 1, and the shape of the recirculating region changes from concave to convex. This pattern of

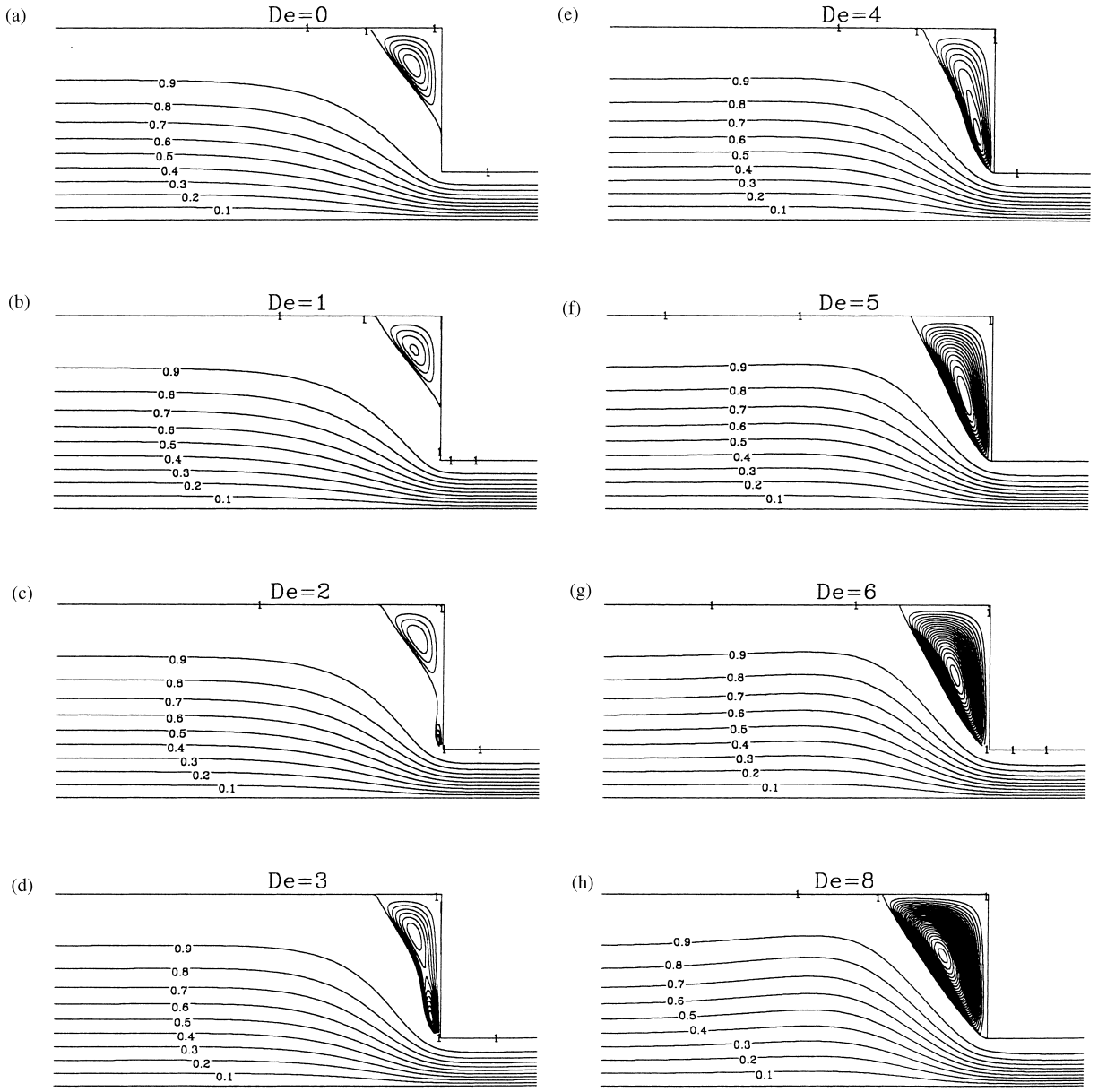

Fig. 4. Predicted streamlines for the UCM fluid at Re = 0.01 in the fine mesh with the UDS scheme. (a) De = 0; (b) De = 1; (c) De = 2; (d) De = 3; (e) De = 4; (f) De = 5; (g) De = 6; (h) De = 8. (Streamlines in the recirculation are equally spaced, with $\delta_\psi = 2 \times 10^{-4}$ for De ≤ 3, and $\delta_\Psi = 5 \times 10^{-4}$ for De > 3).

evolution is in agreement with the experiments of Evans and Walters [4] for high contraction ratios of 16 : 1 and 80 : 1, but is different from what has so far been reported in the literature for the 4 : 1 planar contraction flow of constant viscosity fluids, and this discrepancy raises some questions concerning accuracy, which will be discussed later.

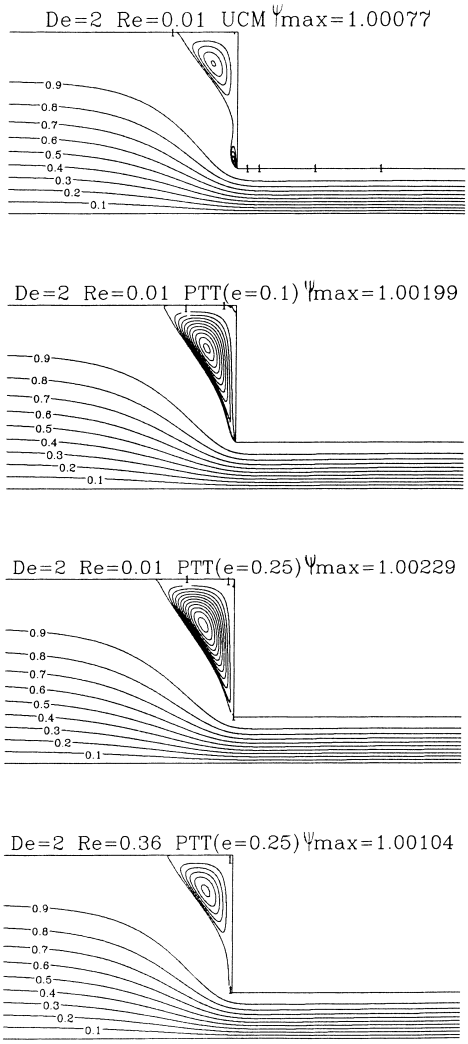

Fig. 5. Comparison of streamline patterns of the UCM and PTT fluids at De = 2. (a) UCM, Re = 0.01; (b) PTT, $\varepsilon = 0.1$, Re = 0.01; (c) PTT, $\varepsilon = 0.25$, Re = 0.01; (d) PTT, $\varepsilon = 0.25$, Re = 0.36. (Streamlines in the recirculation are equally spaced with $\delta_\Psi = 2 \times 10^{-4}$).

In any case, the flow patterns in Fig. 4 closely resemble, for the whole range of Deborah numbers, the visualisations reported by Boger et al. [3] in their axisymmetric experiments with constant viscosity fluids except that the increase in the vortex size is not so accentuated.

Constitutive model effects with special relevance to shear-thinning of the viscosity can be assessed from Fig. 5 where the flow behaviour of the UCM and SPTT fluids are compared for the same Deborah number of 2 and Reynolds numbers of 0.01 and 0.36. For the SPTT model, two different values of the material parameter ε were investigated ($\varepsilon = 0.1$ and 0.25). The main recirculation region for the UCM fluid is rather weak (Fig. 5 (a)), with the stream function being normalised by the incoming flow rate attaining a maximum value of 1.00079 in the salient corner vortex (a relative recirculating intensity of

0.079%), and the salient corner and lip vortices are shown distinctively (the intensity of the latter being 0.06%, giving a total recirculating flow of approximately 0.14%). By reducing the magnitude of the extensional viscosity and introducing shear-thinning behaviour, i.e. increasing ε from 0 to 0.1 in the SPTT model, we observe that a single recirculation zone now spans both the re-entrant and the salient corners and that the maximum value of the normalised stream function has risen to 1.00199, and then to 1.00299 when ε is further increased to 0.25.

A lip vortex is not present for $\varepsilon = 0.1$, but the salient corner eddy has a typical concave shape and extends 'finger-like' up to the re-entrant corner. This eddy becomes less concave and stronger when ε is raised to 0.25. The streamline plots of Baloch et al. [16] are for a higher value of the Reynolds number, namely $\mathrm{Re} = 1$, but have a shape similar to those in Fig. 5 (b). The vortex structures in Fig. 5 compare very well with the equivalent prediction of Xue et al. [18] (c.f. their Figure 19 for $\mathrm{De} = 2.9$). With further increase in ε, Baloch et al's [16] predictions show that the salient corner vortex tends to finger towards the re-entrant corner, a feature not observed in the present study (c.f. Fig. 5 (c)). Again, this feature results from a Reynolds number effect as shown in a comparison between Fig. 5 (c) and Fig. 5 (d), pertaining to $\mathrm{Re} = 0.01$ and 0.36, respectively. Clearly, the flow at a Reynolds number of 0.36 is now similar to that of Baloch et al. [16] for $\mathrm{Re} = 1$, showing that the apparent 'finger pattern' is rather a flattening of the salient corner vortex as it is being pushed towards the contraction wall by inertial forces. This is accompanied by a decrease in the strength of the vortex to a maximum normalised value of the stream function of 1.00104.

Since the ε parameter in the PTT model controls strain-thickening of the elongational viscosity, its effect upon the stress field is manifested in plots of the normal stresses that develop along the centreline in the zone at the entrance to the narrow channel. Fig. 6 (a) shows several longitudinal profiles of the first normal stress difference (N_1) normalised by the respective shear stress at the wall of the downstream channel (T_W) along the axis and in the vicinity of the re-entrant corner, corresponding to the flow cases shown in Fig. 5 (a)–(c). The figure also includes experimental data from Quinzani et al. [8] made non-dimensional in the same way for $\mathrm{De} = 2.9$. The PTT model with $\varepsilon = 0.25$ is found to yield good predictions of the build-up of extensional stresses as the contraction plane is approached, and the rate of decay of N_1/T_W is also well predicted, but not the actual values of N_1. Similar results have been obtained by other authors (e.g. [18]) who simulated the flow measured by Quinzani et al. [34].

Further validation of the present predictions is provided by Fig. 6 (b) where good agreement is seen with the results obtained by Sato and Richardson [23] for the variation in N_1 along the centreline. This case is for $\mathrm{Re} = 1.0$ and $\mathrm{De} = 1$, and the Oldroyd-B predictions of Sato and Richardson do not differ significantly from the present UCM predictions.

In summary, our simulations show that in viscoelastic flow through planar contractions, the mechanism of vortex enhancement is through the formation and the growth of a lip vortex, followed by merging of this vortex and the existing corner vortex and subsequent enhancement of the single remaining vortex. It is noted that this evolution is for a constant Reynolds number, and an increasing Deborah number. In an experiment, as the flow rate is increased for a given fluid, both Re and De increase. The lip vortex at its initial stage, and even when it is already joined with the corner vortex, is small, and so fine meshes are required to resolve it properly and predict its subsequent evolution. This may also explain why the lip vortex is so difficult to observe in experimental work (c.f. [35]). Forthcoming numerical studies using fine meshes and high-order schemes will be required to give more support to the patterns of Fig. 4 for $\mathrm{De} > 4$.

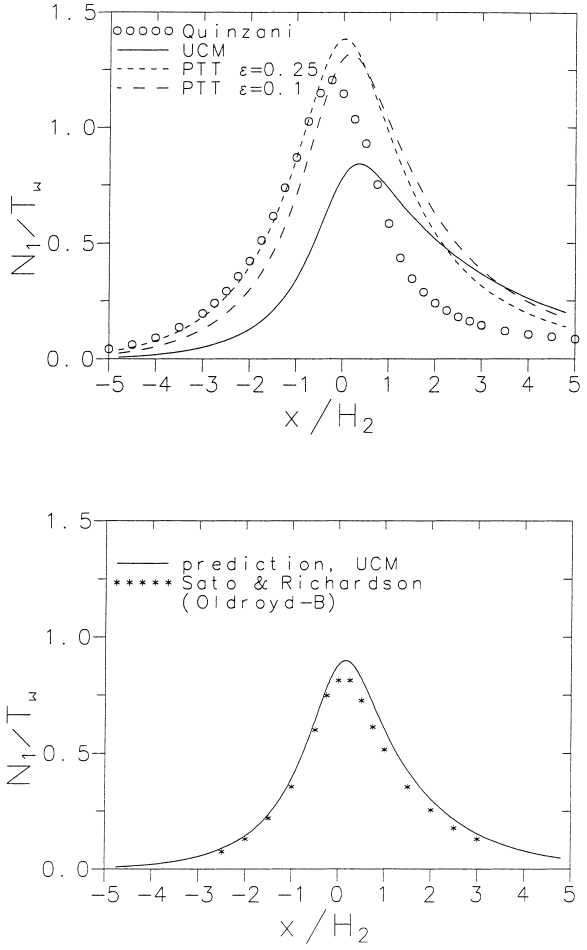

Fig. 6. Longitudinal profile of N_1/T_W along the contraction centreline. (a) comparison with Quinzani et al.'s [8] data; (b) comparison with Sato and Richardson's [23] predictions.

The effect of the Reynolds number is essentially to push the vortex structure against the side-wall, and thus tend to enhance the size of the lip vortex if an envelope structure already exists, as is the case with the Deborah number flows of 2, 3 and 4 in Fig. 4. Therefore, it is important to establish the size and the strength of the vortex pattern, as already noticed in the early work of Yoo and Na [22], but we did not find it to be the decisive factor for the appearance of the lip vortex as suggested by Carew et al. [14], and our results for creeping flow ($Re = 0$) and for $Re = 0.01$ were virtually identical, both exhibiting a lip vortex at $De = 2$. Xue et al. [18] came to the same conclusion.

Our results for Deborah numbers in excess of 4 raise issues of convergence, mesh refinement and accuracy, which are now discussed.

As for convergence, in the sense of iterative convergence to a steady-state solution, all the present results satisfy a tight normalised-residuals criterion of 10^{-4}, i.e. the L_2-norm of the residuals for all equations when appropriately normalised, had fallen below 10^{-4} for a 'converged' steady-state solution to be assumed. Furthermore, the history of these residuals, as the time-stepping 'iterative' procedure

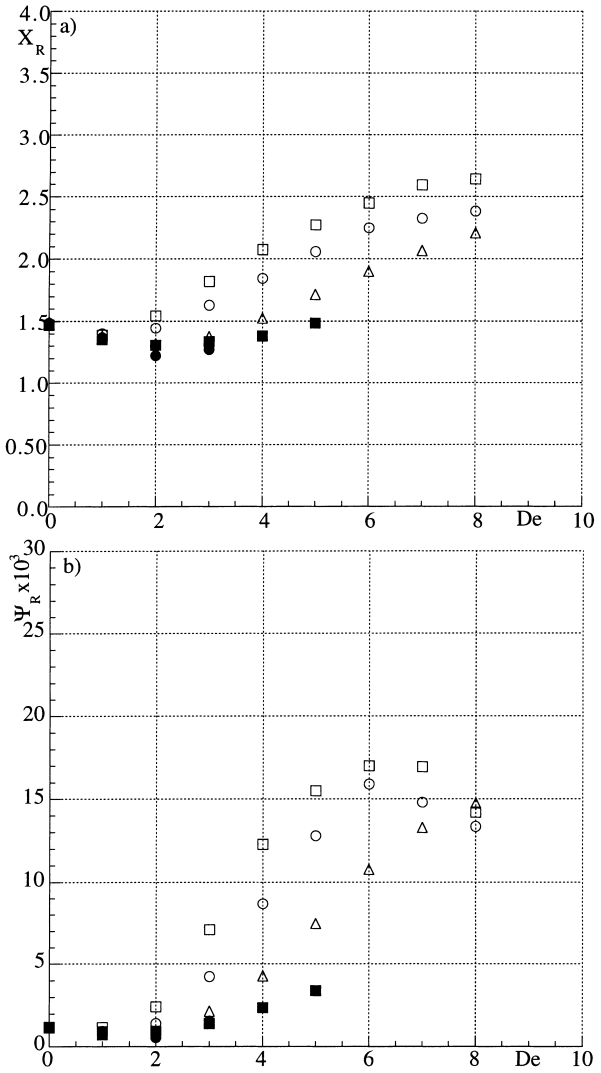

Fig. 7. Effect of mesh fineness and differencing scheme as a function of De at Re = 0.01: □, mesh 1; ○, mesh 2; Δ, mesh 3 (open symbols UDS; closed symbols LUDS). (a) maximum normalised recirculation length (X_R/H_2); (b) maximum normalised stream function ($\Psi_R = \Psi_{max} - 1$).

evolved, was monitored and seen to decay in a frank manner, although not necessarily monotonic for every time step. In order to check these points, the case De = 8 in mesh 3 was restarted from the assumed solution at residuals of 10^{-4} and further advanced to satisfy a criterion of 10^{-6} (here, we note that double-precision arithmetic has been used throughout). Changes in some typical quantities were found to be negligible: Ψ_R x 10^3 changed from 14.7248 to 14.7247 and X_R from 2.207841 to 2.207840.

The importance of mesh refinement is well exemplified by Fig. 7, where the variation in the maximum normalised vortex intensity in the recirculation (Ψ_R), and the vortex size (X_R) for UCM fluids are shown as functions of the Deborah number for different meshes and differencing schemes.

The use of a consistent mesh refinement technique allowed us to apply Richardson's extrapolation to the limit as a method to estimate the accuracy of the predictions.

For the Newtonian case, Richardson's extrapolation based on the three mesh levels allows us to obtain estimated values for X_R and Ψ_R of the fourth- and third-order, respectively, as shown in Tables 3 and 4 where values for all cases are given. The accuracy is measured by the difference between the mesh 3 value and the extrapolated value. For the case De = 1, the variation in X_R in the three meshes is not monotonic, but extrapolation from the two finest meshes still gives a good estimate of X_R. Unfortunately, for higher Deborah numbers, the simultaneous use of the coarse mesh, mesh 1 and a low-order scheme (UDS) renders useless the results with mesh 1 for Richardson's extrapolation, and so it must be based on a two mesh level extrapolation, giving rise to higher inaccuracies, as seen in Tables 3 and 4. The extrapolated values of X_R for De ≥ 2 are, however, of second-order accuracy in spite of the differencing scheme being first-order (c.f. pp. 30–31 of [36]), and the trend shown is again the intensification and increase in the size of the corner vortex. When using LUDS, however, the values of mesh 1 were used for extrapolation, and the accuracy compares the extrapolated and mesh 2 values.

The extrapolation applies better to X_R than to Ψ_R since the flow rates from which Ψ_R is derived are based on the integration of the velocity field and the result is of only zero-order. Thus the estimation of the accuracy has little meaning for Ψ_R when De ≥ 2 and is not given in Table 4. This deterioration of accuracy is very clear in Fig. 7 (b) where the values of Ψ_R in the two coarser meshes start decreasing at high De, contrary to the previous trend. A better estimate of both quantities, and especially of Ψ_R, requires still finer meshes preferably coupled with a higher-order scheme.

In conclusion, the values of the recirculation vortex length of 1.496 and 1.344, for De = 0 and 1, can be used in benchmarking with an estimated accuracy of 0.4%. For De = 2 and 3, we obtain $X_R = 1.19$

Table 3
X_R as a function of the Deborah number and mesh

De	Mesh 1	Mesh 2	Mesh 3	Extrapolated	Accuracy (%)
0					
	1.470[a]	1.488[a]	1.494[a]	1.496	−0.3
1	1.387	1.400	1.378	1.356	1.6
	1.354	1.367	1.350	1.344	0.4
2	1.546	1.443	1.318	1.193	10.5
	1.308	1.222		1.193[c]	2.4
3	1.819	1.628	1.375	1.122	22.5
	1.334	1.268[b]		1.246[c]	1.8
4	2.074	1.845	1.526	1.207	26.4
	1.378				
5	2.274	2.059	1.714	1.369	25.2
	1.485				
6	2.448	2.248	1.899	1.550	22.5
7	2.595	2.325	2.067	1.809	14.3
8	2.641	2.382	2.208	2.034	8.6

First value in each cell is obtained with UDS.
Second value obtained with LUDS.
[a] Second value obtained with CDS.
[b] Second value obtained with 80% LUDS + 20% UDS.
[c] Based on mesh 1 and mesh 2 values.

Table 4
$\Psi_R \times 10^3$ as a function of the Deborah number and mesh

De	Mesh 1	Mesh 2	Mesh 3	Extrapolated	Accuracy [%]
0					
	1.209[a]	1.185[a]	1.164[a]	1.137	2.4
1	1.155	0.948	0.841	0.730	15.2
	0.933	0.832	0.743	0.628	15.5
2	2.401	1.400	0.794	0.188	–
	0.963	0.563	–	–	–
3	7.087	4.234	2.149	0.064	–
	1.429	1.551[b]	–	–	–
4	12.294	8.678	4.276	−0.126	–
	2.355	–	–	–	–
5	15.500	12.804	7.448	2.092	–
	3.386		–	–	–
6	17.003	15.906	10.762	5.618	–
7	16.919	14.796	13.273	11.75	–
8	14.198	13.344	14.725	16.106	–

First value in each cell is obtained with UDS.
Second value obtained with LUDS.
[a] Second value obtained with CDS.
[b] Second value obtained with 80% LUDS plus 20% UDS.

and 1.25, respectively, with accuracy estimates below 2.5%. For higher Deborah numbers, Richardson's extrapolation is useful only in that it indicates that both X_R and Ψ_R tend to increase with De, as the results for the fine mesh show.

The refinement also shows that, in the range $0 \leq De \leq 3$, when a lip vortex is present, the length of the corner vortex remains approximately constant, even decreasing slightly, because all the vortex activity is restricted to the lip vortex. Simultaneously, the discrepancies in the magnitude of the maximum recirculating flow rate are enhanced. In the Deborah number range for which a lip vortex is predicted for the finer mesh, mesh 3 (Fig. 4), Ψ_R turns out to be approximately constant because increased elasticity tends to enhance the lip vortex intensity at the expense of the corner vortex. It is stressed that Ψ_R in Fig. 7 is not the total recirculating flow in the vortices unless there is a single vortex present.

The effect of mesh refinement upon local variables is exemplified in Fig. 8 for $De = 2$. In Fig. 8 (a), we see that the fine mesh, mesh 3, leads to higher and sharper normal stress profiles along the line $y/H_2 = 0.98$ passing nearby the geometric singularity, but the differences with the predictions for mesh 2 are not very significant (less than 5%). Even smaller differences are seen in the velocity profiles of Fig. 8 (b) except in the coarser mesh where some oscillations are seen near the re-entrant corner due to bad resolution coupled with high stress and velocity gradients. Accuracy is also affected by the level of elasticity: Fig. 8 (c) shows the predicted normal stress variations along the centreline for various Deborah numbers in the three meshes. If the stress scale was the same as in Fig. 8 (a), presumably, no discernible differences between the predictions for the two finer meshes would be observed. Even with the enlarged scale of Fig. 8 (c), it is quite clear that the normal stress difference along the contraction centreline is much less sensible to mesh refinement, and one essentially finds mesh-independent results for $De = 2$ and above. However, the important point here is that if fluid elasticity is increased from a De

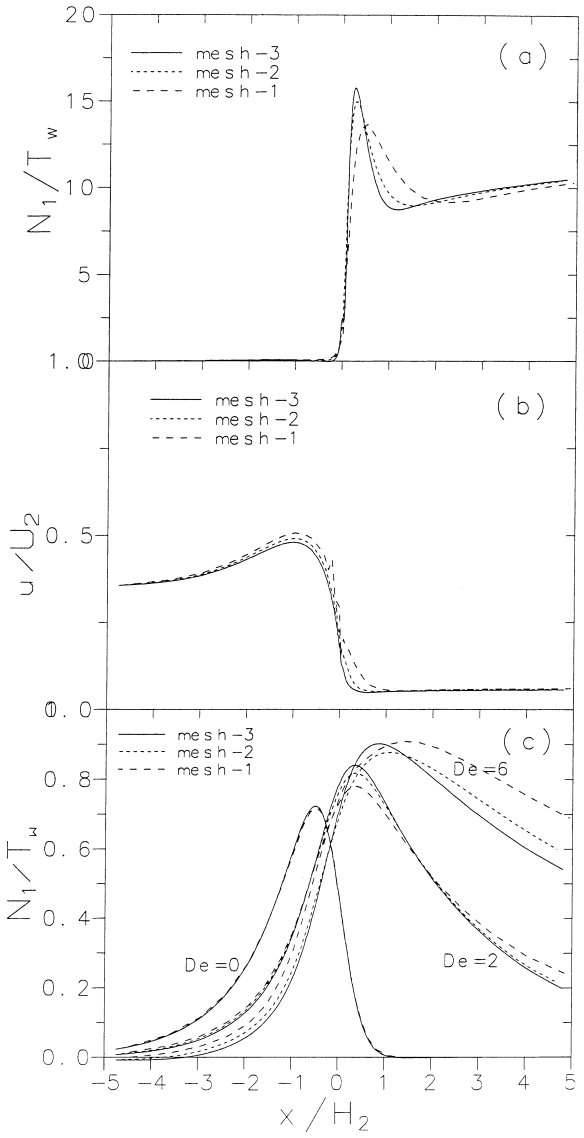

Fig. 8. Effect of mesh refinement on the longitudinal profiles of (a) N_1/T_W at $y/H_2 = 0.98$; (b) u/U_2 at $y/H_2 = 0.98$; (c) N_1/T_W at $y/H_2 = 0$.

of 2 to 6, then mesh 1 is clearly inadequate for resolving the N_1 evolution along the centreline. Hence, in numerical predictions of highly elastic fluids, the computational meshes have to be significantly finer than those which were adequate for less elastic fluids. The difference between the N_1 values for mesh 3 and mesh 2 are less than 3.5% at De = 6 along the centreline, but will be larger near the salient corner.

The computational meshes used in the present work are much finer than those used by Marchal and Crochet [12], even when considering that their finite elements possess additional internal points and, in fact, their results resemble our predictions when these are produced with coarser meshes. However, it is already apparent that the coarse mesh results are too inaccurate (c.f. Fig. 7). The effect of mesh

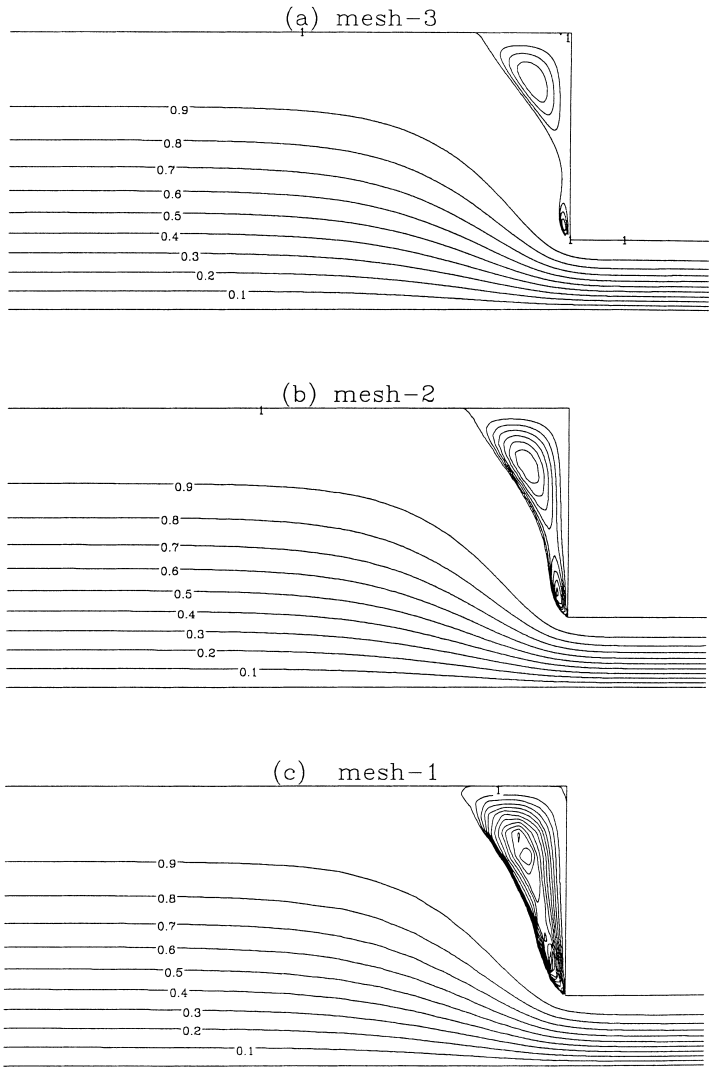

Fig. 9. Effect of mesh refinement on the flow pattern of the UCM fluid at De = 2. (a) fine mesh; (b) medium mesh; (c) coarse mesh; ($\delta_\Psi = 2 \times 10^{-4} \equiv$ streamline spacing in the recirculation).

refinement can be assessed again in the streamline plots of Fig. 9 which refers to the UCM fluid flow at a Reynolds number of 0.01 and a Deborah number of 2. In the finer mesh, separation between the lip and corner vortices is clearly seen, although the two are already enveloped by the separation streamline ($\Psi = 1$), in agreement with the prediction of Matallah et al. ([15], c.f. Figure 2) for the better recovery scheme and also with Xue et al. ([18], see Figure 8, in mesh M4). With the two other meshes, the corner vortex intensity is artificially enhanced (by 76% in mesh 2 and 200% in mesh 1), and in the coarser mesh, the two vortices are almost merged. These differences in flow patterns are purely a consequence of the refinement of the mesh used, and the flow field which is a solution to the differential equations is obviously unique and is expected to be closer to that shown in Fig. 9 (a).

The issue of mesh refinement has also been addressed by Xue et al. [18], and the deterioration in the predictions for flow pattern observed here with coarser meshes is very similar to the results given in their Figure 8 (b). Note, however, that in the present work, the smallest mesh spacing was still 40% finer than that in the finest mesh of Xue et al. [18] who used 8379 nodes (in the overall domain, including the portions outside the flow domain), and so the number of cells in our fine mesh exceeds their's by more than 200%. Our ability to use very fine meshes is a result of the indirect-addressing capability of the method, which allows significant memory savings.

Mesh refinement and/or use of higher-order differencing schemes are the two ways of improving numerical accuracy. We now turn attention to this second issue. It is well known that the first-order upwind scheme introduces numerical diffusion and this fact has been felt in this work (c.f. Fig. 7). It is emphasised that for the Reynolds number considered here (from $Re \approx 0.01$ up to unity), numerical diffusion is confined to the convective terms in the constitutive equations and is absent from the convective terms in the momentum equations. In fact, it has been checked that the results were virtually identical for Newtonian fluids using either UDS or LUDS. Fig. 10 shows streamline plots obtained with the medium and coarse sized grids using the second-order accurate LUDS for $De = 2$ and $Re = 0.01$. These plots should be compared with those produced with UDS and plotted in Fig. 9.

The beneficial effects of the higher-order differencing scheme are remarkable: now, even the coarser mesh (Fig. 10 (a)) gives rise to a flow pattern very close to that of the fine mesh, a conclusion already apparent in the results given in Fig. 7. The drawback, already noted, is that convergence is more difficult to attain with the LUDS scheme and thus it was found easier to obtain accurate converged

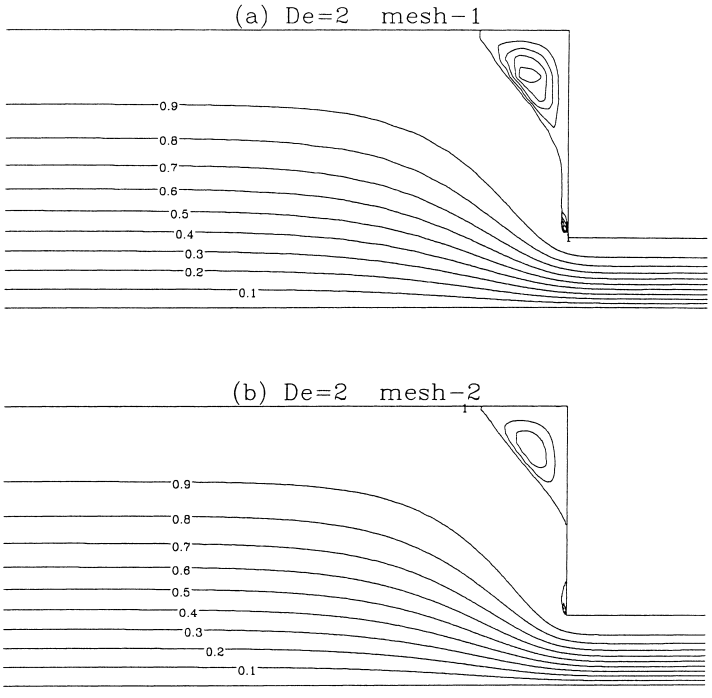

Fig. 10. Flow pattern of the UCM fluid at $De = 2$ and $Re = 0.01$ using LUDS: (a) in the coarse mesh, mesh 1; (b) in the medium mesh, mesh 2.

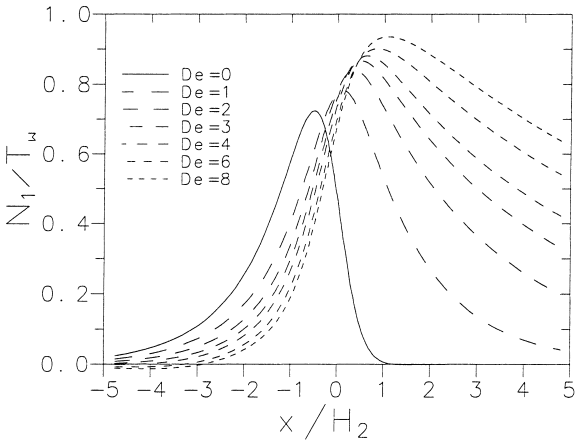

Fig. 11. Longitudinal profile of N_1/T_W along the centreline as a function of the Deborah number at Re = 0.01.

solutions using a much finer grid together with the UDS scheme. Future work will have to deal with this matter of procuring numerical stability with higher-order schemes.

Finally, we present in Fig. 11 the centreline variation in N_1/T_W as a function of the Deborah number for the UCM fluid (for which $T_W = 3\eta U_2/H_2$ at a Reynolds number of 0.01. Increasing the De number raises the maximum value of N_1/T_W, although not dramatically, certainly because the shape of the vortices adjusts in such a way as to minimise the stresses. The main effect is that those high stress values are preserved over a longer distance downstream of the contraction plane due to the convective influence in the constitutive equations, and the sharp rise in N_1/T_W tends to be shifted to the contraction plane and into the entrance region of the smaller channel.

6. Conclusions

A general FV method based on the collocated mesh arrangement and indirect addressing was applied to the prediction of the flow of UCM and SPTT fluids with varying degrees of strain-thickening and elongational viscosity and flowing in the 4 : 1 planar sudden contraction geometry. Both nominally first- and second-order accurate discretization schemes were used for the convective terms. The base case had a Reynolds number of 0.01 and the Deborah number varied from 0 to 8. The analysis of the effect of mesh refinement upon the accuracy of the results benefitted from the application of Richardson's extrapolation to the limit technique. No special artifacts, such as extra diffusion in the stress equation, were necessary for obtaining converged solutions with the finer computational meshes used in the calculations.

The predicted flow patterns for the UCM fluid showed all the complex features seen in flow visualisations of constant-viscosity fluid in circular contraction [3] and of shear-thinning fluids in plane contraction [5]. As De is increased at constant Re, a lip vortex appears, grows and connects to the corner vortex through a fingering and enveloping process until a single vortex remains with its centre closer to the lip. Thereafter, further increase in De produces a standard vortex enhancement picture. The fact remains that the appearance of the lip vortex is not supported by existing experimental evidence. It

is, however, supported by the very recent numerical simulations of Matallah et al. [15] and Xue et al. [18,19] who used different numerical methods (finite-element and finite-volume, respectively). These authors did not pursue their calculations for higher De numbers, and thus did not cover the upper range of De where the single remaining vortex grows. This issue still requires further investigation, in particular, confirmation with finer meshes and higher-order differencing schemes for the convective terms in the constitutive equations. The higher-order differencing scheme utilised here has, however, shown lack of robustness, failing to converge for moderate Deborah numbers in the finer meshes. Converged solutions for the second-order linear upwind scheme were obtained in all meshes only for $De \leq 1$, and in the coarse mesh, mesh 1, for De up to 5. Even in this coarse mesh, the predictions for LUDS approached those for the UDS in the finer mesh, mesh 3. The vortex features are very sensitive to mesh refinement and the present results for the vortex size have an estimated accuracy below 25% at high Deborah numbers and show vortex enhancement for De greater than 3. Benchmarking X_R data is given for $De = 0$, 1, 2 and 3. For higher De, the estimated accuracy rises to $\approx 25\%$.

The predictions with the simplified PTT model fluid ($\varepsilon \neq 0$, $\xi = 0$) were also in agreement with previously reported findings for the same fluid, thus confirming the capability of the present FV method in dealing with complex constitutive equations in geometries possessing singularities.

Acknowledgements

Both authors would like to acknowledge the financial support of project PBIC/P/QUI/1980/95 of JNICT-Junta Nacional de Investigação Científica e Technológica, and F. T. Pinho also acknowledges the partial financial support from the Stichting fund of Schlumberger. The kindness of Professor Lidia Quinzani in providing tabulated data of her experimental measurements is gratefully recorded here. The authors are listed alphabetically.

References

[1] D.V. Boger, Viscoelastic flows through contractions, Ann. Rev. Fluid Mech. 19 (1987) 157.
[2] L.M. Quinzani, R.C. Armstrong, R.A. Brown, Use of coupled birefringence and LDV studies of flow through a planar contraction to test constitutive equations for concentrated polymer solutions, J. Rheology 39 (1995) 1201.
[3] D.V. Boger, D.U. Hur, R.J. Binnington, Further observations of elastic effects in tubular entry flows, J. Non-Newtonian Fluid Mech. 20 (1986) 31.
[4] R.E. Evans, K. Walters, Flow characteristics associated with abrupt changes in geometry in the case of highly elastic liquids, J. Non-Newtonian Fluid Mech. 20 (1986) 11.
[5] R.E. Evans, K. Walters, Further remarks on the lip-vortex mechanism of vortex enhancement in planar-contraction flows, J. Non-Newtonian Fluid Mech. 32 (1989) 95.
[6] D.M. Binding, An approximate analysis for contraction or converging flows, J. Non-Newtonian Fluid Mech. 27 (1988) 173.
[7] S.A. White, D.G. Baird, Flow visualization and birefringence studies on planar entry flow behavior of polymer melts, J. Non-Newtonian Fluid Mech. 29 (1988) 245.
[8] L.M. Quinzani, R.C. Armstrong, R.A. Brown, Birefringence and laser-Doppler velocimetry studies of viscoelastic flow through a planar contraction, J. Non-Newtonian Fluid Mech. 52 (1994) 1.
[9] S.A. White, D.G. Baird, Numerical simulation studies of the planar entry flow of polymer melts, J. Non-Newtonian Fluid Mech. 30 (1988) 47.

[10] M.J. Crochet, G. Pilate, Plane flow of a fluid of second grade through contractions, J. Non-Newtonian Fluid Mech. 1 (1976) 247.
[11] M.G.N. Perera, K. Walters, Long range memory effects involving abrupt changes in geometry Part II: The expansion/contraction/expansion, J. Non-Newtonian Fluid Mech. 2 (1977) 191.
[12] J.M. Marchal, M.F. Crochet, A new mixed finite element for calculating viscoelastic flow, J. Non-Newtonian Fluid Mech. 26 (1987) 77.
[13] D. Rajagopalan, R.C. Armstrong, R.A. Brown, Finite element methods for calculations of steady viscoelastic flow using constitutive equations with a Newtonian viscosity, J. Non-Newtonian Fluid Mech. 36 (1990) 159.
[14] E.O.A. Carew, P. Townsend, M.F. Webster, A Taylor–Petrov–Galerkin algorithm for viscoelastic flow, J. Non-Newtonian Fluid Mech. 50 (1993) 253.
[15] H. Matallah, P. Townsend, M.F. Webster, Recovery and stress-splitting schemes for viscoelastic flows, J. Non-Newtonian Fluid Mech. 75 (1998) 139.
[16] A. Baloch, P. Townsend, M.F. Webster, On the simulation of highly elastic complex flows, J. Non-Newtonian Fluid Mech. 59 (1995) 111.
[17] B. Purnode, M. Crochet, Flows of polymer solutions through contractions Part 1: Flows of polyacrylamide solutions through planar contractions, J. Non-Newtonian Fluid Mech. 65 (1996) 269.
[18] S.-C. Xue, N. Phan-Thien, R.I. Tanner, Three dimensional numerical simulations of viscoelastic flows through planar contractions, J. Non-Newtonian Fluid Mech. 74 (1998) 195.
[19] S. Xue, N. Phan-Thien, R.I. Tanner, Numerical investigations of Lagrangian unsteady extensional flows of viscoelastic fluids in 3-D rectangular ducts with sudden contractions, Rheol. Acta 37 (1998) 158.
[20] P.J. Oliveira, F.T. Pinho, The plane contraction flow of upper convected Maxwell fluids calculated by a finite-volume collocated-mesh method, V Encontro Nacional de Mecânica Computacional 2 (1997) 987.
[21] S.H. Song, J.Y. Yoo, Numerical simulation of viscoelastic flow through a sudden contraction using a type dependent difference method, J. Non-Newtonian Fluid Mech. 24 (1987) 221.
[22] J.Y. Yoo, Y. Na, A numerical study of the planar contraction flow of viscoelastic fluids using the SIMPLER algorithm, J. Non-Newtonian Fluid Mech. 39 (1991) 89.
[23] T. Sato, S. Richardson, Explicit numerical simulation of time-dependent viscoelastic flow problems by a finite element/finite volume method, J. Non-Newtonian Fluid Mech. 51 (1994) 249.
[24] J.M. Marchal, M.F. Crochet, Hermitian finite elements for calculating viscoelastic flow, J. Non-Newtonian Fluid Mech. 20 (1986) 187.
[25] P.J. Oliveira, F.T. Pinho, G.A. Pinto, Numerical simulation of non-linear elastic flows with a general collocated finite-volume method, J. Non-Newtonian Fluid Mech. 79 (1998) 1.
[26] R.G. Larson, Constitutive equations for polymer melts and solutions, Butterworths, Boston, USA, 1988.
[27] G. Astarita, G. Marrucci, Principles of Non-Newtonian Fluid Mechanics, McGraw-Hill, New York, USA (Maidenhead, UK), 1974.
[28] S.V. Patankar, Numerical Heat Transfer and Fluid Flow, Hemisphere Publishing Corporation, Washington, DC, USA, 1980.
[29] C.M. Rhie, W.L. Chow, A numerical study of the turbulent flow past an isolated airfoil with trailing adge separation, AIAAJ 21 (1983) 1525–1532.
[30] G.P. Sasmal, A finite volume approach for calculation of viscoelastic flow through an abrupt axisymmetric contraction, J. Non-Newtonian Fluid Mech. 56 (1995) 15.
[31] K.A. Missirlis, D. Assimacopoulos, E. Mitsoulis, A finite volume approach in the simulation of viscoelastic expansion flows, J. Non-Newtonian Fluid Mech. 78 (1998) 91.
[32] R.I. Issa, P.J. Oliveira, Numerical predictions of phase separation in two-phase flow through T-junctions, Computers and Fluids 23 (1994) 347.
[33] J.P. Van Doormal, G.D. Raithby, Enhancements of the SIMPLE method for predicting incompressible fluid flows, Num. Heat Transfer 7 (1984) 147.
[34] J.H. Ferziger, M. Perić, Computational Methods for Fluid Dynamics, Springer, Berlin, Germany, 1996.
[35] B. Tremblay, Visualization of the flow of low density polyethylene/polystyrene blends through a planar step contraction, J. Non-Newtonian Fluid Mech. 52 (1994) 323.
[36] J.H. Ferziger, Numerical Methods for Engineering Application, Wiley, New York, USA, 1981.